

Structurally Integrated Properties of Random, Uni-Directional, and Bi-Directional Freeze-Dried Cellulose/Chitosan Aerogels

Aneeba Chaudary

Donghua University - Songjiang Campus: Donghua University

Mohammed Kayes Patoary

Donghua University - Songjiang Campus: Donghua University

Meiling Zhang

Donghua University - Songjiang Campus: Donghua University

Tayba Chudhary

Zhejiang University

Amjad Farooq

Donghua University - Songjiang Campus: Donghua University

Lifang Liu (✉ lifangliu@dhu.edu.cn)

Donghua University <https://orcid.org/0000-0002-0315-2048>

Research Article

Keywords: Biomass aerogels, Cellulose nanofibers, Chitosan, Customized freezing techniques, Thermal insulation, Mechanical properties

Posted Date: September 28th, 2021

DOI: <https://doi.org/10.21203/rs.3.rs-893477/v1>

License: © ⓘ This work is licensed under a Creative Commons Attribution 4.0 International License.

[Read Full License](#)

Abstract

Aerogels as a thermally insulating material have attracted extensive consideration in recent years due to prevailing energy consumption in building, industrial sector, and aerospace applications. Cellulose contains all the favorable properties to be used as a thermally resistant substance but due to structural instability, it needs to be impregnated with other resilient substances. We report herein the preparation of cellulose nanofiber (CNF)/chitosan (CS) isotropic and anisotropic composite aerogels (CCSA) by employing three different: random, uni-directional, and bi-directional freezing techniques, ensuing freeze-drying process to investigate the structural modification effect on the thermal and mechanical properties. Aerogels behaved distinctively along different axis due to holding entirely eccentric porous micro-orientation along lateral (perpendicular to ice growth) and axial (parallel to ice growth) directions. Randomly frozen aerogels (r-CCSA) contained uneven porous networks because of random ice crystal formation within the microstructure and resulted in isotropic characteristics with thermal conductivity (λ) of $0.038 \text{ Wm}^{-1}\text{K}^{-1}$ in both axial and radial direction. whereas unidirectional frozen aerogels (u-CCSA) exhibited anisotropic microstructure and performance with lamellas in axial and honeycombed in radial direction resulting in λ value of $0.040 \text{ Wm}^{-1}\text{K}^{-1}$ and $0.034 \text{ Wm}^{-1}\text{K}^{-1}$ respectively. Similarly, the controlled temperature gradient during the preparation of bidirectional aerogels (b-CCSA) presented an anisotropic sheet-like microstructure and resulted in ultra-low thermal conductivity along the axial and radial geometry with λ of $0.033 \text{ Wm}^{-1}\text{K}^{-1}$ and $0.027 \text{ Wm}^{-1}\text{K}^{-1}$ respectively because of the Knudsen effect. CCSA reported in this work resulted in ultra-low density (5 to 16 mgcm^{-3}), high porosity ($\sim 99.6\%$), and robustness mechanically with an endurance of 60% strain. Such a composite bio-mass aerogel preparation method will offer a clear insight into the adoption of the right methodology according to target practical applications with consideration of environmental safety.

1. Introduction

Thermal insulation is an important factor for energy-efficient buildings, space applications, and greenhouse gas emissions (Zhang et al. 2019). Since thermally insulating materials need to be porous to minimize heat flow and environmentally friendly to address biocompatibility, plenty of commercial insulating materials have been fabricated e.g., expanded polystyrene with λ of $\sim 0.035 \text{ Wm}^{-1}\text{K}^{-1}$, rock wool, and glass fibers with thermal conductivity (λ) of $0.15 \text{ Wm}^{-1}\text{K}^{-1}$ to $0.53 \text{ Wm}^{-1}\text{K}^{-1}$. However, it requires high thickness to meet the target insulation value. Vacuum insulation panels with λ of $0.030 \text{ Wm}^{-1}\text{K}^{-1}$ to $0.040 \text{ Wm}^{-1}\text{K}^{-1}$, but can easily damage while handling (Alam et al. 2011). Conversely, aerogels are the materials obtained from the gel after supercritical drying to preserve gel morphology, composed of 95–99% air with average pore size $< 20 \text{ nm}$, high specific surface area, and lower density $< 0.1 \text{ g/cm}^3$ (Yahya et al. 2020), which makes them the best choice for thermal insulation (Apostolopoulou-Kalkavoura et al. 2020; Jiang et al. 2020; Sakuma et al. 2021). Silica-based aerogels with λ of 0.018 to $0.042 \text{ Wm}^{-1}\text{K}^{-1}$ have been fabricated for achieving better thermal insulation (Zhao et al. 2015a; Guo et al. 2021; Xiao et al. 2021; Xue et al. 2021); however, due to their brittleness and processing complexity, the application areas of silica-based aerogels are restricted (Zhao et al. 2015b; Rigacci et al. 2017).

Polysaccharides such as cellulose nanofiber-based aerogels, due to their unique characteristics, such as high specific surface area, low density, great mechanical strength, high porosity, low thermal conductivity, presence of a large number of functional groups, biodegradability, and natural renewability (Dufresne 2017; Lavoine and Bergström 2017; Ahankari et al. 2021a) has engrossed increasing interest as a potential and sustainable replacement for thermal insulation (Ahankari et al. 2021b; Han et al. 2021), environmental (Lavoine and Bergström 2017), energy (Fan et al. 2021), and biomedical applications (Zhang et al. 2020a). Thermal insulation is an attractive property to target nowadays for environmental interest, as studies have been conducted to reduce the thermal conductivity of CNF aerogels by making their composites with other substantial materials (Zhang et al. 2020a; Liu et al. 2021; Zuo and Yuan 2021). Such an approach helps in the reduction of heat radiation caused by carbonaceous materials. Another naturally most abundant bio-based polymer, chitosan (CS), holding many amino and hydroxyl groups, is a desirable material for plenty of application areas. However, low mechanical strength and functionalization can be reinforced with other high mechanical and thermally insulating materials (Alhwaige et al. 2016; Zhang et al. 2021). For example, cellulose-chitosan reinforced aerogels for thermal insulation (Zhang et al. 2020b), chitosan-nano fibrillated cellulose (CS-NFC) composite aerogels for oil/water separation (Li et al. 2018; Zhang et al. 2018), carbon-chitosan composites for CO₂ adsorption (Alhwaige et al. 2016), graphene-chitosan aerogels for water purification by removing heavy metal ions (Hu et al. 2020), and many more.

Aerogels behave differently on varying structural morphology (Hu et al. 2020), and this structural orientation can diverge by modifying pore structure within aerogels' geometry after employing various freeze casting techniques and by changing freezing velocity and temperature. He et al. (2020a) fabricated boehmite hydrosols and alumina nanopowder aerogel by adopting different freezing temperatures and observed the relationship between ice front rate (v) and structural wavelength (λ) variations. Random freeze aerogels exhibit randomly distributed porous microstructure, non-linear sensitivity, and unsatisfactory mechanical performance. Whereas, a controlled freeze-casting environment produces well-ordered anisotropic aerogels, which behave specifically along a different axis due to anisotropic behavior. These aerogels have broad environmental applications according to obligatory end-use.

Many studies have been conducted in recent years to obtain desired thermal (Munier et al. 2020; Zou and Budtova 2021), mechanical (Sun et al. 2020), high water content (Qian et al. 2020), CO₂ adsorption (Wei et al. 2020), electromagnetic interference shielding (Deng et al. 2021), electrification, and shape recovery (Li et al. 2020), as well as oil/water separation (Cao et al. 2021) properties by adopting anisotropic freeze casting methodology in the preparation of aerogels. For instance, He et al. (2020b) adopted the uni-directional freeze-drying technique and observed different thermal and mechanical behavior by changing direction along perpendicular and parallel to ice-crystals. Qin et al. (2021) fabricated carbon nanofibre/transition metal carbides and carbonitrides hybrid aerogels employing a uni-directional freezing technique and found enhanced reversible compressibility and structural stability of final aerogels. Similarly, Maleki et al. Dou et al. (2019) prepared ceramic-based hybrid aerogels with high thermal stability by adopting the directional freezing methodology. For better thermal insulation

properties and high shielding efficiency, the use of anisotropic aerogels is an excellent choice (Apostolopoulou-Kalkavoura et al. 2020; Chen et al. 2020; Garemark et al. 2020; Su et al. 2020; Cao et al. 2021; Liu et al. 2021).

This study adopted three different random, uni-directional, and bi-directional freezing strategies to fabricate CNF/CS-based isotropic and anisotropic composite aerogels to observe the structurally integrated characteristics along a different axis. Formaldehyde was used as a crosslinker for chemical bonds formation between CNF and CS in the hydrogel phase, and sublimation was done following the freeze-drying technique. As CNF acts as a structural reinforcing nanofiller for the biopolymer chitosan aerogel, we investigated the effect of structural modification due to the adoption of each methodology on the final aerogels' characteristics. We evaluated micro-orientation, physical properties, thermal behavior, compressibility, elasticity to demonstrate the structural modification effect on resultant properties. The lowest thermal conductivity value was obtained for anisotropic aerogels employing the bi-directional freezing technique was $0.027 \text{ Wm}^{-1}\text{K}^{-1}$ in the radial direction, which is quite less than the isotropic thermal insulating aerogels. Therefore, the relative adoption of the best suitable preparation route according to practical applications would be easy to understand.

2. Experimental

2.1. Materials

2,2,6,6-tetramethylpiperidine oxide (TEMPO) generated CNF with a concentration of 1.2% were provided by Tianjin Lontec Biopharma Co. Ltd. CS was purchased from Shanghai Titan technology Co., Ltd. Formaldehyde from Sinopharm Chemical Reagent Co., Ltd. (Shanghai, China). Acetic Acid, sodium hydroxide, and formaldehyde were provided by Shanghai Aladdin Reagent Co., Ltd. All chemicals were analytically pure.

2.2. Preparation of hydrogel

The aqueous solution of CNF with a weight percent of 0.3% (C_3) and 0.7 wt% (C_7) was prepared by adding deionized water into TEMPO-CNF suspension, which dispersed and homogenized at 14,000 rpm with the aid of a high-speed homogenizer (Ultra-Turrax, IKA) for 30–35 min. Meanwhile, CS solutions have been prepared by mixing CS by 0.3 wt% (CS_3), 0.7 wt% (CS_7), 1 wt% (CS_{10}) wt%, and 1.2 (CS_{12}) wt% ratios with 0.1 M glacial acetic acid following continuous magnetic stirring in 80°C heated oil bath for 40 min to obtain a transparent and uniform suspension. CNF dispersions (C_3 & C_7) were further mixed individually with the prepared chitosan ratios (CS_3 , CS_7 , CS_{10} , and CS_{12}) while vigorous stirring for an additional 30 min to get a proper dispersed viscous suspension. The resultant composite solution named as C_3CS_3 , C_3CS_7 , C_3CS_{10} , C_3CS_{12} , C_7CS_3 , C_7CS_7 , C_7CS_{10} and C_7CS_{12} respectively (Figure S1). Once thoroughly mixed, the pH was raised to 7 by adding a subsequent amount of NaOH. 0.2% (v/v) formaldehyde was added to the final hydrogel and let the solution on magnetic attiring for 5h for cross-linking process and final hydrogel formation.

2.3. Fabrication of aerogels following distinct freezing techniques

The CNF/CS hydrogel poured into a plastic mold and directly placed into liquid nitrogen (-196 °C) bath for freezing, following lyophilizing process for 2 consecutive days at -50 °C using freeze dryer under 1Pa vacuum pressure, as prepared aerogels named as randomly freeze-dried CNF/CS aerogels (r-CCSA).

For directional freezing technique, the hydrogel suspension was transferred into PTFE (polytetrafluoroethylene) mold while placing on a copper square bar in the liquid nitrogen-filled bath for 20 min and lyophilized for 60 hours, as prepared aerogels named unidirectional-CNF/CS aerogels (u-CCSA).

Surface bioinspired structure aerogels prepared by transferring complex suspension into a customized PDMS (polydimethylsiloxane) wedge square mold with a bottom slope angle of about 20° and immersed into liquid nitrogen for about 45 min ensuring absolute freezing. The frozen hydrogel was then lyophilized for 72 hours; aerogels were further kept in a vacuum oven at 100 °C for 60 min for well cross-linking. Surface bioinspired structured aerogels prepared using this procedure named bidirectional-CNF/CS aerogels (b-CCSA).

2.4. Characterization

The microscopic architecture of CCSA was analyzed by SEM (Hitachi S-4800), the compression experiments were conducted using Instron 5944 universal machine with 500-N load cells using a strain rate of 2mm min⁻¹ with 60% strain. The weight of CCSA was obtained using an ultra-micro balance (MS105DU, Mettler Toledo). The chemical structure was observed conducting FTIR testing with spectra range 4000 to 400 cm⁻¹ in transmission mode on the resolution of 4 cm⁻¹. Thermal conductivity obtained using Hot Disk thermal analyzer (TPS2500S) following transient plane source (TPS) method. Infrared images of aerogels were captured using a thermal infrared camera (Testo 868); thermal stability of aerogels was studied by a thermogravimetric analyzer (PerkinElmer Inc., USA) with a 20 ml/min nitrogen flow rate with a temperature range of 30 to 600 °C and heating rate 10 °C /min. Shrinkage of aerogels was obtained from volume to size of the mold ratio. Porosity values calculated using the following expression:

$$P = \left(1 - \frac{\rho_0}{\rho}\right) \times 100$$

Where P represents porosity, ρ_0 apparent density, and ρ skeletal density, here we use the average density of CNF (1.46 g/cm³) and CS (1.75 g/cm³) to get the final skeletal density.

3. Results And Discussion

3.1. Structurally integrated functionality

CNF was blended with CS to fabricate isotropic (random) and anisotropic (uni-directional, bidirectional) composites aerogels by pouring CNF/CS suspension into the customized molds following the sol-gel method and freeze-drying, as shown in Fig. 1a-c. The adoption of three different freezing techniques generates three different cross-linked CNF/CS composite aerogel's (CCSA) interfacial assembly, as shown in Fig. 1d. CCSAs were manufactured using a lower and higher concentrated CNF suspension, with gradually increasing CS amount to study the properties and composition effect accordingly. To study the structural orientations and their ultimate effects on final properties, we adopted three criteria while preparing CCSA: (I) randomly oriented pore structure-based aerogels (r-CCSA), (II) Controlled porous assembly oriented uni-directional anisotropic aerogels (u-CCSA), and (III) bio-inspired 3D ordered morphology attaining bi-directional composite aerogels (b-CCSA).

In this regard, three different freeze-drying techniques were employed. For attaining the first criteria, we used the conventional freeze-drying method in which CNF/CS hydrogel poured into a flat rounded plastic mold following direct freezing into liquid nitrogen flow; in this process, the temperature gradient was not specified, so the final aerogels' morphology consisted of random pores distribution along the both axial (longitudinal) and radial (cross-sectional) direction. The structure of r-CCSA is illustrated in Fig. 2a-c. As shown in Fig. 2a, the low concentrated CNF/CS made aerogel exposed a less stable microstructure with wide pore size and uneven geometric distribution. On the other hand, C₇CS₇A structure (Fig. 2b-c) showed a compact morphology with an obvious pore wall in the sampling plane (Fig. 2 inset) with an average pore size of 12 to 20 μm in both axial and radial direction. The inset of Fig. 2c showing the evident presence of CNF on pore walls.

To meet the second criterion-the CNF/CS hydrogel was poured into PTFE mold and frozen by placing on a copper bar in liquid nitrogen, following the freeze-drying process. Because of a controlled temperature gradient, the ice crystals formation occurs, and a sublimation process left anisotropic morphology without affecting the parent structure. The longitudinal section of u-CCSA (Fig. 2e and inset) exhibited parallel lamellar cell geometry with lamellas spacing around 20–30 μm. This geometry of aerogels formed due to water crystallization induction along the axis, which ultimately allowed nanofibers and chitosan particles to form an organized sheet structure.

Chitosan is a substance that provided skeletal stability by forming bridge bands between lamellas (Fig. 2f and inset), which ultimately enhanced the mechanical strength of final aerogels. However, the lower concentration of CS (C₇CS₃A) made aerogels displayed irregular geometric structure (Fig. 2d) with a lamellar distance around 35 to 55 μm. A nanoscale observation of u-CCSA exhibited microfibers of CNF on the walls of lamellas (Figure S3a). It can also be noted that the lamellar structure of u-CCSA possesses a unique macro-anisotropic orientation within the cellular geometry which ultimately results in the anisotropic thermal conductivity and mechanical behavior of final aerogels (Figure S2).

Lastly, the bi-directional aerogels were prepared by pouring the sol-gel into a customized mold followed by freeze-drying and cross-linking. The structure made from this technique is presented in Fig. 2g-i; the parallel layered orientation of the structure is quite visible along the longitudinal direction and

honeycombed along the cross-sectional. This specific structure was induced because of a defined temperature gradient along the length of aerogels (vertically by PDMS wedge) and with the PDMS wedge (horizontally); as a result, the ice crystallization behaved differently. Figure 2h and inset presents aligned lamellar structure of b-CCSA axially, containing a layer gap of about 20 to 30 μm . While the cross-sectional view also contains a clear presentation of individual layers and shows the anisotropic geometry of aerogels (Fig. 2i and inset). A nanoscale observation of b-CCSA shows the evidence of cellulose nanofibers on the wall of lamellas see Figure S3b. The lower concentration of cellulose and chitosan containing b-CCSA (C_7CS_3A) having non-solid geometry of lamellas with layers gap of about 35 to 40 μm (Fig. 2g).

3.2. Characterization of physical properties at room temperature

Composite CNF/CS aerogels has been prepared by mixing CNF with a concentration of 0.3% and 0.7% (C_3 and C_7) individually with CS solution of 0.3%, 0.7%, 1%, and 1.2% for C_3CS_3A , C_3CS_7A , $C_3CS_{10}A$, $C_3CS_{12}A$, C_7CS_3A , C_7CS_7A , $C_7CS_{10}A$ and $C_7CS_{12}A$ aerogels formation respectively. Mechanical behavior within random aerogels is mentioned with “r-CCSA,” and anisotropic aerogels (uni-directional and bidirectional) represented with “u,b-CCSA” in Fig. 3 for comparison purposes. A digital photograph of lightweight CCSA with a volume of $\sim 12\text{cm}^3$ is shown in Fig. 3a, which indicates its ultra-low density. Fig. 3b displays a linear increase in densities with a gradual increase of CS ratio. The increase of CS concentration from 0.3% to 0.7% in CNF suspension increased the aerogel density value up to 30%. In contrast to C_7CS_7 , upon 1% CS addition in C_7CS_{10} , the density decreased by 7% because of the formation of porous structure stability within aerogels. However, an appropriate amount of CS (0.7% to 1%) is suitable for better density to mechanical strength proportion achievement. The porosity value in r- C_3CS_7A and u-b- C_3CS_7A decreased with the addition of 1% CS in C_7CS_{10} . While the CS addition gradually increased the porosity value in C_7CS_3A , C_7CS_7A , and $C_7CS_{10}A$ which decreased when the CS ratio exceeded up to 1.2% (Fig. 3c).

The optimum CS content fulfills the structural defects and stabilizes the porous structure of aerogels. A CS ratio of 1.2% enhances the solid content within the confined geometry, which ultimately results in pores reduction inside the aerogel fibril walls. The volume shrinkage was reduced to 37–48% on the addition of CS to 0.3% (C_3CS_3 and C_7CS_3) in pure CNF aerogels and further reduced to 24% with 0.7–1% CS addition. But when this ratio reaches 1.2%, the volume shrinkage increased up to 30% (Fig. 3d) because an optimum CS addition strengthened the interaction between microfibers and kept the 3D solid network structure locked onto the position through which porous structure was not affected.

Figure 3e shows the FTIR spectra of CNF, CS, and CCSA. The characteristic peaks at 3351cm^{-1} , 2893cm^{-1} correspond to $-\text{OH}$, $\text{C}-\text{H}$ bonds respectively (Peng et al. 2016). The peak at around 3351cm^{-1} is stretching vibrations of $-\text{OH}$ and $-\text{NH}$. The peak in chitosan aerogels at 1644cm^{-1} corresponds to the amide group. However, in composite aerogels, the new peak at 1470cm^{-1} formed after cross-linking

reaction, corresponding to the amide bond formation between formaldehyde and chitosan. In composite aerogels, the sharp peak at $\sim 1690\text{cm}^{-1}$ is evidence of cross-linked aerogels corresponding to aldehyde group formation (Yagoub et al. 2019). Formaldehyde addition to aerogels develops structural stability and enhances the mechanical strength of final aerogels by providing strengthening units within the micro-orientation of aerogels.

3.3. Thermal stability of the CNF/CS aerogels

Thermal stability is essential for thermal insulation applications. The TGA (Fig. 4a) and DTG (Fig. 4b) results display the thermal degradation of CNF, CS, and composite CCSA. There were four weight loss stages of CCSA aerogels. The first weight-loss phase begins around $100\text{ }^{\circ}\text{C}$, which could be attributed to the absorbed water from aerogels. The second stage was in the range of $200\text{--}350\text{ }^{\circ}\text{C}$, the organic component's decomposition. The third weight-loss of raw CCSA was observed between $400\text{--}450\text{ }^{\circ}\text{C}$, and the final weight-loss occurs because of the removal of structural water and carbonization between $500\text{--}600\text{ }^{\circ}\text{C}$. The pure CNF aerogels decomposed at $279\text{ }^{\circ}\text{C}$ with mass retention of 12.6%. However, with an appropriate amount of CNF and CS ratio within aerogel, the degradation temperature (T_g) increased from $282\text{ }^{\circ}\text{C}$ ($\text{C}_3\text{CS}_7\text{A}$) to $300\text{ }^{\circ}\text{C}$ ($\text{C}_7\text{CS}_7\text{A}$), and the weight loss of CCSA was also reduced from $\sim 90\%$ to $\sim 70\%$. Compared to the pure CNF aerogels, the mass retention rate increased up to 54% for $\text{C}_7\text{CS}_3\text{A}$ and up to 84% for $\text{C}_7\text{CS}_7\text{A}$, which shows the CS content helped in the thermal stability of the CCSA. It can be seen in Table 1 the chitosan aerogels having great T_g , so with the addition of CS to CNF aerogels, a physical barrier formed within the structure consisting of nanosheets that prevent composite aerogel from combustion.

Table 1
Thermal degradation of CCSA at different ratios

| Sample | T_g ($^{\circ}\text{C}$) | Weight loss (%) | Final retention (%) |
|---------------------------------|---------------------------------|--------------------|---------------------|
| CNF | 279 | 87.4 | 12.6 |
| CS | 310 | 70.4 | 29.6 |
| $\text{C}_3\text{CS}_3\text{A}$ | 291.7 | 93.7 | 6.2 |
| $\text{C}_3\text{CS}_7\text{A}$ | 282.6 | 93.1 | 6.9 |
| $\text{C}_7\text{CS}_3\text{A}$ | 286 | 80.5 | 19.5 |
| $\text{C}_7\text{CS}_7\text{A}$ | 299.5 | 76.7 | 23.3 |

3.4. Thermal conductivity

The anisotropy of thermal conductivity (λ) correlates with the morphology of the porous structure formed as a result of the adoption of three different freezing processes (as mentioned in Fig. 1 earlier). The λ has been observed along all three directional aerogels (Fig. 5g, h, and i), and the values were compared for pure aerogels and composite aerogels on different ratios (Figure S4). Schematic illustration of CCSA microstructure is represented in Fig. 5a-f represents the microstructure of all three directional aerogels individually. As can be seen, r-CCSA shows similar morphology along the radial (Fig. 5a) and axial directions (Fig. 5b). This random porous structure allows maximum thermal heat conduction through the pores, which ultimately maximizes the λ . While the directional freeze aerogels (uni and bi-CCSA) hold an anisotropic skeleton, which lowers the heat localization in a radial direction and controls heat transfer in the lateral one (Fig. 5c-f). As the layered structure of anisotropic aerogels greatly minimizes the thermal conduction, (Su et al. 2020) it has been observed that for pure CNF-axial/lateral, the thermal conductivity was $0.031 \text{ Wm}^{-1}\text{K}^{-1}/0.024 \text{ Wm}^{-1}\text{K}^{-1}$ and CS-axial/lateral were $0.035 \text{ Wm}^{-1}\text{K}^{-1}/0.031 \text{ Wm}^{-1}\text{K}^{-1}$ (see Fig S4a,b). Conversely, the composite aerogels, r-CCSA (axial/lateral), u-CCSA (axial/lateral), and b-CCSA (axial/lateral) the λ were $0.038 \text{ Wm}^{-1}\text{K}^{-1}/0.038 \text{ Wm}^{-1}\text{K}^{-1}$, $0.040 \text{ Wm}^{-1}\text{K}^{-1}/0.034 \text{ Wm}^{-1}\text{K}^{-1}$ and $0.033 \text{ Wm}^{-1}\text{K}^{-1}/0.027 \text{ Wm}^{-1}\text{K}^{-1}$ respectively.

SEM images of u-CCSA reveal the cellular structure of aerogels with long pore channel alignment with cross-bridges in longitudinal direction allows the heat to spread along with the spaces by preventing heat localization upon the accumulation of thermal energy in the sample. Whereas honeycombed pore orientation in the cross-sectional area provides a wide surface area for heat to float in, which reduces solid heat conduction and prevents quick heat flow through the aerogels. However, the b-CCSA samples freeze in a customized mold with a dual temperature gradient shows the lowest thermal conductivity values compared to the previous two techniques. The lamellar structure reduces heat convection, conduction, and radiation, eventually reducing the whole thermal conductivity value. Whereas, along the longitudinal direction of b-CCSA, the heat can float through the channels easily due to the absence of connecting medium between lamellas, resulting in more thermal conduction.

The concentration of cellulose and chitosan also affect the thermal conductivity values. The thermal conductivity of aerogels has been shown to have a direct relationship with their densities (Zou and Budtova 2021). So that with the lower concentration of CNF (C_3), composite aerogels $C_3\text{CS}_3\text{A}$, $C_3\text{CS}_{10}\text{A}$ and $C_3\text{CS}_{12}\text{A}$ expressed λ value of $0.027 \text{ Wm}^{-1}\text{K}^{-1}$, $0.025 \text{ Wm}^{-1}\text{K}^{-1}$ and $0.036 \text{ Wm}^{-1}\text{K}^{-1}$ respectively (see Fig S4c). Thermal conductivity value first decreased to 8% with the addition of CS_{10} , and it increased to 44% when CS_{12} content was enhanced from a certain level due to exhibiting a higher density of $C_3\text{CS}_{12}\text{A}$. Likewise higher CNF (C_7) comprising CCSA aerogels $C_7\text{CS}_3\text{A}$, $C_7\text{CS}_{10}\text{A}$ and $C_7\text{CS}_{12}\text{A}$ attained λ of $0.035 \text{ Wm}^{-1}\text{K}^{-1}$, $0.031 \text{ Wm}^{-1}\text{K}^{-1}$ and $0.038 \text{ Wm}^{-1}\text{K}^{-1}$ respectively. The λ value first decreased by 11% and then increased to 22%; this increase in thermal conductivity can be attributed to $C_7\text{CS}_{12}\text{A}$'s higher density.

The λ was ($0.027 \text{ Wm}^{-1}\text{K}^{-1}$ to $0.036 \text{ Wm}^{-1}\text{K}^{-1}$), which is less than the highly concentrated composite aerogels ($0.032 \text{ Wm}^{-1}\text{K}^{-1}$ to $0.040 \text{ Wm}^{-1}\text{K}^{-1}$) because of the density variation. Whereas with increasing

chitosan ratio up to an optimum range ($C_3CS_{10}A$ and $C_7CS_{10}A$), λ decreased from $\sim 7\%$ to $\sim 13\%$, whereas with higher concentration ($C_3CS_{12}A$ and $C_7CS_{12}A$), the λ increased drastically up to $\sim 7\%$ to $\sim 18\%$. This variation of thermal conductivity occurred because CS minimized the structural defects up to a certain level, while the addition of more solid contents into the assembly affected the pore structure, which caused an increase in thermal conduction (Zhang et al. 2021).

3.5. Thermal Insulation Mechanism

Thermographic images of nano-composites aerogels have been captured using an infrared camera (Fig. 6a) by keeping the CNF, CS, and CCSA samples of 10 mm thickness on a hot stage while maintaining the temperature at 200 °C. Infrared images from the side of samples were taken with each 5 min time intervals for 60 min, and the temperature difference (Δt) between the hot stage and aerogels' surface has been summarized in Fig. 6b. It was revealed that the temperature flow along the random aerogels was quite fast, with a temperature increase of 31% after 1-hour exposure to the heat. The corresponding temperature distribution along pure CNF and CS aerogels can be seen in Figure S5.

Conversely, along anisotropic aerogels, the heat flow in a radial direction is comparatively slower than the lateral ones, with a temperature increase of 7% and 28%, respectively. Moreover, by reducing the anisotropic CCSA's thickness from 20 mm to 5 mm, the surface temperature remains 64 °C with a stage temperature of 200 °C, expressing the good heat resistance property of aerogels even on smaller thicknesses (Fig. 6c).

The heat transfer mechanism is described in Fig. 6d-i. The heat transfer in porous materials occurs in various modes, such as solid conduction, gas conduction, convection, and radiation. The heat transfer by convection is negligible because of the smaller pore size of aerogels (< 1 mm) (Apostolopoulou-Kalkavoura et al. 2020). Conversely, the radiation is negligible at ambient temperature and pressure for the lower density and porous materials. However, the gas conduction (due to collision of gas molecules) contributes to heat transfer along the aerogels at ambient atmosphere, and it depends on the mean free path and pore size of material, but gas conduction is relatively lower when the pore size is smaller than mean free path of air molecules as per Knudsen effect. In anisotropic aerogels (Fig. 6f&h), the CNF/CS particles are well-aligned within channels along the axial direction. The lateral heat conduction (brown dotted lines) within the aerogel assembly is much faster than the radial direction. Moreover, higher temperature and oxygen content make heat convection (green dotted lines) and heat radiation (red dotted line) quicker to flow along the axial path. Because of the wide opening of channels, most CNF and CS particles were exposed to high temperatures, which induced quicker heat flow in the axial direction than the lateral one. Figure 6g&i illustrates the heat flow of u & b-CCSA in an axial and lateral direction. The lamellas are at a distance in u-CCSA but connected with bridge bands which ultimately let the heat conduction transfer through this assembly. However, the micro-channels are not interconnected in b-CCSA radially and do not provide enough room to let heat through accessible space with any possible mean, which reduces the temperature flow eventually.

3.6. Mechanical property analysis

To evaluate the mechanical properties of CCSA, a compression test was conducted using the universal testing machine. The resulting stress-strain curve of CNF, CS, and their composite aerogels along the radial and axial direction is illustrated in Fig. 7. The stress-strain curve of aerogels tested along axial direction exhibits a typical compression behavior consisting of three distinctive regimes: (i) the linear elastic stage at low strain, (ii) plateau beyond the yield point, and (iii) final densification region at compressive strain over 60% (Song et al. 2018; Wang et al. 2019). In random freeze aerogels, stress-strain behavior is similar along with both directions and exhibits low compressive strength because of disordered porous orientation. The compression along a radial direction of both uni and bi-directional aerogels (Fig. 7c and e) do not exhibit an apparent linear regime before the plateau. However, a unique anisotropic mechanical behavior can be observed for bidirectional aerogels when compressed along the axial direction (Fig. 7d), because of its highly ordered microstructure. As presented in Fig. 7a, c, and e, the aerogels compressed in the direction parallel to lamellas express good elasticity. Along the direction parallel to lamellas, aerogels are difficult to bend and exhibit good compressive strength (see Figure S6a, b, and e).

As shown in Fig. 7f with increasing CNF and CS ratios, Young's modulus (E) and yield strength (Fig. 7g) increased significantly along an axial direction. Young's modulus increased to 175% on increasing CS content from 0.3 to 0.7 within the lower concentration of CNF suspension and up to 56% along axial direction when CS content increased up to an optimum range in higher concentrated CNF suspension (C₇CS₇A). While yield strength reached 100% for C₃CS₇A aerogels and 20% for C₇CS₇A relatively. Furthermore, a cyclic compression test on 60% strain was conducted for anisotropic aerogels in the radial direction for 5 consecutive cycles (Fig. 7h); these aerogels could withstand the compressive strain of 60% and recovered to their original shape by 75% after the release of cyclic stress, Fig. 7i shows the recovery rate after each cycle completion, this result expresses the good elasticity and structural robustness of anisotropic CNF/CS composite aerogels.

For better understanding, the CNF/CS composite aerogels were prepared to adopt three different freezing techniques, which affected resultant morphology and properties. The CCSA aerogels fabricated by employing random freeze methodology consisted of compact fibrous assembly with irregular pore size and isotropic properties along with both axial and radial directions. Meanwhile, uni-directional CCSA grasped lamellar geometry with bridge support between, showed anisotropic micro-orientation and properties along an axial and radial direction. Whereas CCSAs prepared by adopting bi-directional freezing technique shown the detached layered assembly of CCSA after freeze-drying and cross-linking. However, b-CCSA presented the best physical, thermal, and compressive strength properties along the radial direction compared to other polymeric aerogels (Cai et al. 2020; Zhou et al. 2020; Yan et al. 2021; Zuo and Yuan 2021), and more elasticity and compress recovery in axial alignment (Video S2).

4. Conclusion

In summary, three different structurally oriented CNF/CS composite aerogels are fabricated at different ratios, using formaldehyde crosslinker by employing three random, uni-directional, and bidirectional

freeze casting strategies. Chitosan served as a structural reinforcing component and reduced the volume shrinkage rate of aerogels from 40–16% while curtailing structural defects and improving the orientation of pores, which ultimately improved the macroscopic stability of CCSA with high porosity (~ 99.6%), lowest density (5–16 mg/cm³) and 60% strain endurance. Optimized CNF to CS (C₇CS₇ to C₇CS₁) ratios defined the stable microporous structure of CCSA over crosslinking by formaldehyde. The r-CCSA presented identical properties with the random pores distribution all over the structure holding pores size of 12 to 20 μm and comparatively high thermal conductivity (λ) along the axial (0.038Wm⁻¹K⁻¹) and radial (0.038Wm⁻¹K⁻¹) orientation. u-CCSA presents anisotropic performance with lamellas spacing of 20–30 μm and λ value 0.040 Wm⁻¹K⁻¹/0.034 Wm⁻¹K⁻¹ along the axial/radial orientation respectively. Whereas, b-CCSA exhibited anisotropic performance as well with containing a layer gap of about 20 to 30 μm and λ value of 0.33 Wm⁻¹K⁻¹/0.027 Wm⁻¹K⁻¹ along the axial/radial direction respectively, due to controlled temperature gradient. The desired characteristics of high thermal insulation, mechanical robustness, and environmental friendliness achieved by adopting adequate preparation techniques make aerogels an appropriate and safe choice for effective thermal insulation applications in construction, aerospace, materials, and extreme environmental conditions.

Declarations

Author Contribution

The manuscript was written through the contributions of all authors. Aneeba Chaudary carried out the experiments and accomplish writing work; Mohammed Kayes Patoary, Meiling Zhang, Tayba Chudhary and Amjad Farooq provided language help during writing; Lifang Liu helped in writing and proofreading the manuscript. All authors have approved the final version of the manuscript.

Acknowledgments

This work was supported by the National Key R&D Program of China (Project No. 2018YFC2000900).

Conflict of interest

The authors declare no conflict of interest.

Declarations

Not Applicable.

References

1. Ahankari S, Paliwal P, Subhedar A, Kargarzadeh H (2021a) Recent Developments in Nanocellulose-Based. <https://doi.org/10.1021/acsnano.0c09678>

2. Ahankari S, Paliwal P, Subhedar A, Kargarzadeh H (2021b) Recent Developments in Nanocellulose-Based Aerogels in Thermal Applications: A Review. *ACS Nano* 15:3849–3874. <https://doi.org/10.1021/acsnano.0c09678>
3. Alam M, Singh H, Limbachiya MC (2011) Vacuum Insulation Panels (VIPs) for building construction industry–A review of the contemporary developments and future directions. *Appl Energy* 88:3592–3602
4. Alhwaige AA, Ishida H, Qutubuddin S (2016) Carbon aerogels with excellent CO₂ adsorption capacity synthesized from clay-reinforced biobased chitosan-polybenzoxazine nanocomposites. *ACS Sustain Chem Eng* 4:1286–1295
5. Apostolopoulou-Kalkavoura V, Munier P, Bergström L (2020) Thermally Insulating Nanocellulose-Based Materials. *Adv Mater* 2001839. <https://doi.org/10.1002/adma.202001839>
6. Cai C, Wei Z, Huang Y et al (2020) Ultralight Programmable Bioinspired Aerogels with an Integrated Multifunctional Surface for Self-Cleaning, Oil Absorption, and Thermal Insulation via Coassembly. *ACS Appl Mater Interfaces*. <https://doi.org/10.1021/acscami.0c00308>
7. Cao M, Li SL, Cheng JB et al (2021) Fully bio-based, low fire-hazard and superelastic aerogel without hazardous cross-linkers for excellent thermal insulation and oil clean-up absorption. *J Hazard Mater* 403:123977. <https://doi.org/10.1016/j.jhazmat.2020.123977>
8. Chen Y, Zhang L, Mei C et al (2020) Wood-Inspired Anisotropic Cellulose Nanofibril Composite Sponges for Multifunctional Applications. *ACS Appl Mater Interfaces* 12:35513–35522. <https://doi.org/10.1021/acscami.0c10645>
9. Deng Z, Tang P, Wu X et al (2021) Superelastic, Ultralight, and Conductive Ti₃C₂T_x MXene/Acidified Carbon Nanotube Anisotropic Aerogels for Electromagnetic Interference Shielding. *ACS Appl Mater Interfaces* 13:20539–20547. <https://doi.org/10.1021/acscami.1c02059>
10. Dou L, Zhang X, Cheng X et al (2019) Hierarchical Cellular Structured Ceramic Nanofibrous Aerogels with Temperature-Invariant Superelasticity for Thermal Insulation. *ACS Appl Mater Interfaces* 11:29056–29064. <https://doi.org/10.1021/acscami.9b10018>
11. Dufresne A (2017) *Handbook of Nanocellulose and Cellulose Nanocomposites*
12. Fan FR, Wang R, Zhang H, Wu W (2021) Emerging beyond-graphene elemental 2D materials for energy and catalysis applications. *Chem Soc Rev*. <https://doi.org/10.1039/c9cs00821g>
13. Garemark J, Yang X, Sheng X et al (2020) Top-Down Approach Making Anisotropic Cellulose Aerogels as Universal Substrates for Multifunctionalization. *ACS Nano* 14:7111–7120. <https://doi.org/10.1021/acsnano.0c01888>
14. Guo JF, Tang GH, Jiang Y-G et al (2021) Inhibited radiation transmittance and enhanced thermal stability of silica aerogels under very-high temperature. *Ceram Int*
15. Han X, Ding S, Fan L et al (2021) Janus biocomposite aerogels constituted of cellulose nanofibrils and MXenes for application as single-module solar-driven interfacial evaporators. *J Mater Chem A*. <https://doi.org/10.1039/d1ta04991g>

16. He F, Li W, Yang L et al (2020a) Alumina aerogels with unidirectional channels under different freezing temperatures during freeze casting—Part I: Control and analysis of pore channels. *Ceram Int* 46:13588–13598
17. He F, Zhu Z, Yang L et al (2020b) Alumina aerogels with unidirectional channels under different freezing temperatures during freeze casting—Part II: Anisotropic mechanical and thermal conductive properties. *Ceram Int* 46:25691–25696. <https://doi.org/10.1016/j.ceramint.2020.07.045>
18. Hu J, Zhu J, Ge S et al (2020) Biocompatible, hydrophobic and resilience graphene/chitosan composite aerogel for efficient oil – water separation. *Surf Coatings Technol* 385:125361
19. Jiang S, Zhang M, Jiang W et al (2020) Multiscale nanocelluloses hybrid aerogels for thermal insulation: The study on mechanical and thermal properties. *Carbohydr Polym* 247:116701. <https://doi.org/10.1016/j.carbpol.2020.116701>
20. Lavoine N, Bergström L (2017) Nanocellulose-based foams and aerogels: Processing, properties, and applications. *J Mater Chem A* 5:16105–16117. <https://doi.org/10.1039/c7ta02807e>
21. Li D, Wang Y, Long F et al (2020) Solvation-Controlled Elastification and Shape-Recovery of Cellulose Nanocrystal-Based Aerogels. *ACS Appl Mater Interfaces* 12:1549–1557. <https://doi.org/10.1021/acsami.9b18569>
22. Li Z, Shao L, Hu W et al (2018) Excellent reusable chitosan/cellulose aerogel as an oil and organic solvent absorbent. *Carbohydr Polym* 191:183–190
23. Liu C, Wan L, Li Q et al (2021) Ice-Templated Anisotropic Flame-Resistant Boron Nitride Aerogels Enhanced through Surface Modification and Cellulose Nanofibrils. *ACS Appl Polym Mater* 3:1358–1367. <https://doi.org/10.1021/acsapm.0c01219>
24. Munier P, Apostolopoulou-Kalkavoura V, Persson M, Bergström L (2020) Strong silica-nanocellulose anisotropic composite foams combine low thermal conductivity and low moisture uptake. *Cellulose* 27:10825–10836. <https://doi.org/10.1007/s10570-019-02912-0>
25. Peng H, Wu J, Wang Y et al (2016) A facile approach for preparation of underwater superoleophobicity cellulose/chitosan composite aerogel for oil/water separation. *Appl Phys A Mater Sci Process* 122:1–7. <https://doi.org/10.1007/s00339-016-0049-0>
26. Qian C, Higashigaki T, Asoh TA, Uyama H (2020) Anisotropic Conductive Hydrogels with High Water Content. *ACS Appl Mater Interfaces* 12:27518–27525. <https://doi.org/10.1021/acsami.0c06853>
27. Qin L, Yang D, Zhang M et al (2021) Superelastic and ultralight electrospun carbon nanofiber/MXene hybrid aerogels with anisotropic microchannels for pressure sensing and energy storage. *J Colloid Interface Sci* 589:264–274. <https://doi.org/10.1016/j.jcis.2020.12.102>
28. Rigacci A, Budtova T, Smirnova I (2017) Aerogels: a fascinating class of materials with a wide potential of application fields. *J Sol-Gel Sci Technol* 84:375–376. <https://doi.org/10.1007/s10971-017-4538-1>
29. Sakuma W, Yamasaki S, Fujisawa S et al (2021) Mechanically Strong, Scalable, Mesoporous Xerogels of Nanocellulose Featuring Light Permeability, Thermal Insulation, and Flame Self-Extinction. *ACS Nano*. <https://doi.org/10.1021/acs.nano.0c08769>

30. Song J, Chen C, Yang Z et al (2018) Highly compressible, anisotropic aerogel with aligned cellulose nanofibers. *ACS Nano* 12:140–147
31. Su L, Wang H, Niu M et al (2020) Anisotropic and hierarchical SiC@SiO₂ nanowire aerogel with exceptional stiffness and stability for thermal superinsulation. *Sci Adv* 6:1–10. <https://doi.org/10.1126/sciadv.aay6689>
32. Sun H, Bi H, Lin X et al (2020) Lightweight, anisotropic, compressible, and thermally-insulating wood aerogels with aligned cellulose fibers. *Polymers (Basel)* 12:. <https://doi.org/10.3390/polym12010164>
33. Wang K, Liu X, Tan Y et al (2019) Two-dimensional membrane and three-dimensional bulk aerogel materials via top-down wood nanotechnology for multibehavioral and reusable oil/water separation. *Chem Eng J* 371:769–780
34. Wei J, Geng S, Hedlund J, Oksman K (2020) Lightweight, flexible, and multifunctional anisotropic nanocellulose-based aerogels for CO₂ adsorption. *Cellulose* 27:2695–2707. <https://doi.org/10.1007/s10570-019-02935-7>
35. Xiao Y, Li L, Cai H et al (2021) In situ co-polymerization of high-performance polybenzoxazine/silica aerogels for flame-retardancy and thermal insulation. *J Appl Polym Sci* 138:50333
36. Xue T, Fan W, Zhang X et al (2021) Layered double hydroxide/graphene oxide synergistically enhanced polyimide aerogels for thermal insulation and fire-retardancy. *Compos Part B Eng* 219:108963
37. Yagoub H, Zhu L, Shibraen MHMA et al (2019) Complex aerogels generated from nano-polysaccharides and its derivatives for oil-water separation. *Polymers (Basel)* 11:. <https://doi.org/10.3390/polym11101593>
38. Yahya EB, Alzalouk MM, Alfallous KA, Abogmaza AF (2020) Antibacterial cellulose-based aerogels for wound healing application: A review. *Biomed Res Ther* 7:4032–4040. <https://doi.org/10.15419/bmrat.v7i10.637>
39. Yan M, Pan Y, Cheng X et al (2021) “Robust – Soft” Anisotropic Nano fibrillated Cellulose Aerogels with Superior Mechanical, Flame-Retardant, and Thermal Insulating Properties. <https://doi.org/10.1021/acsami.1c05334>
40. Zhang H, Li Y, Shi R et al (2018) A robust salt-tolerant superoleophobic chitosan/nanofibrillated cellulose aerogel for highly efficient oil/water separation. *Carbohydr Polym* 200:611–615
41. Zhang J, Cheng Y, Tebyetekerwa M et al (2019) “Stiff–soft” binary synergistic aerogels with superflexibility and high thermal insulation performance. *Adv Funct Mater* 29:1806407
42. Zhang M, Jiang S, Han F et al (2021) Anisotropic cellulose nanofiber/chitosan aerogel with thermal management and oil absorption properties. *Carbohydr Polym* 264:118033
43. Zhang Y, Yin C, Cheng Y et al (2020a) Electrospinning Nanofiber-Reinforced Aerogels for the Treatment of Bone Defects. *Adv wound care* 9:441–452. <https://doi.org/10.1089/wound.2018.0879>
44. Zhang Z, Tan J, Gu W et al (2020b) Cellulose-chitosan framework/polyaniline hybrid aerogel toward thermal insulation and microwave absorbing application. *Chem Eng J* 395:125190

45. Zhao S, Malfait WJ, Demilecamps A et al (2015a) Strong, thermally superinsulating biopolymer-silica aerogel hybrids by cogelation of silicic acid with pectin. *Angew Chemie* 127:14490–14494
46. Zhao S, Zhang Z, Sèbe G et al (2015b) Multiscale assembly of superinsulating silica aerogels within silylated nanocellulosic scaffolds: improved mechanical properties promoted by nanoscale chemical compatibilization. *Adv Funct Mater* 25:2326–2334
47. Zhou S, Apostolopoulou-Kalkavoura V, Tavares da Costa MV et al (2020) Elastic Aerogels of Cellulose Nanofibers@Metal–Organic Frameworks for Thermal Insulation and Fire Retardancy. *Nano-Micro Lett* 12:1–13. <https://doi.org/10.1007/s40820-019-0343-4>
48. Zou F, Budtova T (2021) Polysaccharide-based aerogels for thermal insulation and superinsulation: An overview. *Carbohydr Polym* 266:118130. <https://doi.org/10.1016/j.carbpol.2021.118130>
49. Zuo B, Yuan B (2021) Flame-retardant cellulose nanofiber aerogel modified with graphene oxide and sodium montmorillonite and its fire-alarm application. *Polym Adv Technol* 32:1877–1887. <https://doi.org/10.1002/pat.5231>

Figures

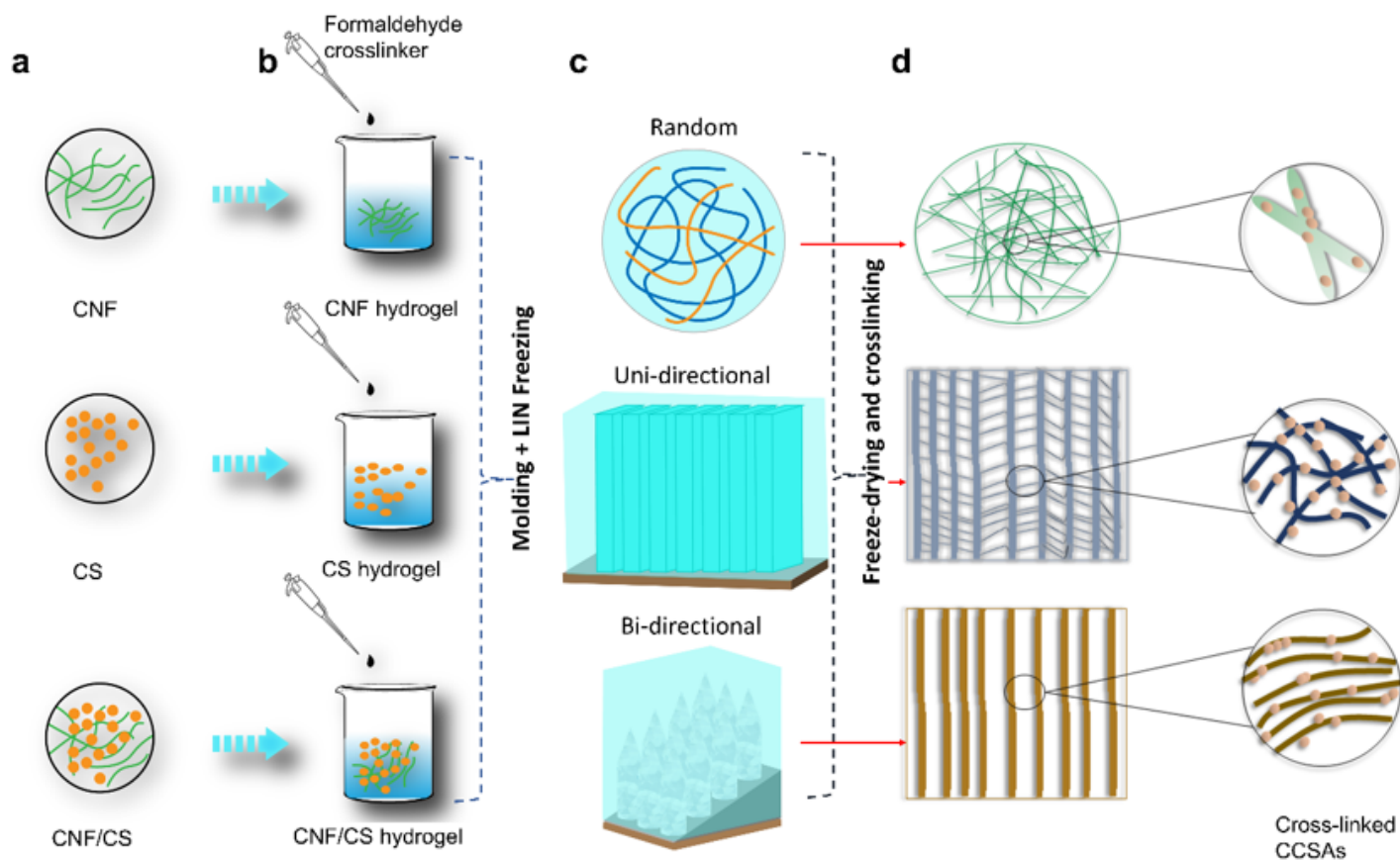


Figure 1

Schematic illustration for preparation method of CNF/CS aerogels including; a CNF chains and CS particles suspension. b Hydrogel formation upon addition of crosslinker and magnetic stirring. c Schematic illustration of CNF/CS suspension frozen in random, uni-directional, and customized bidirectional molds. d Interfacial assembly formation of all three kinds of CCSAs

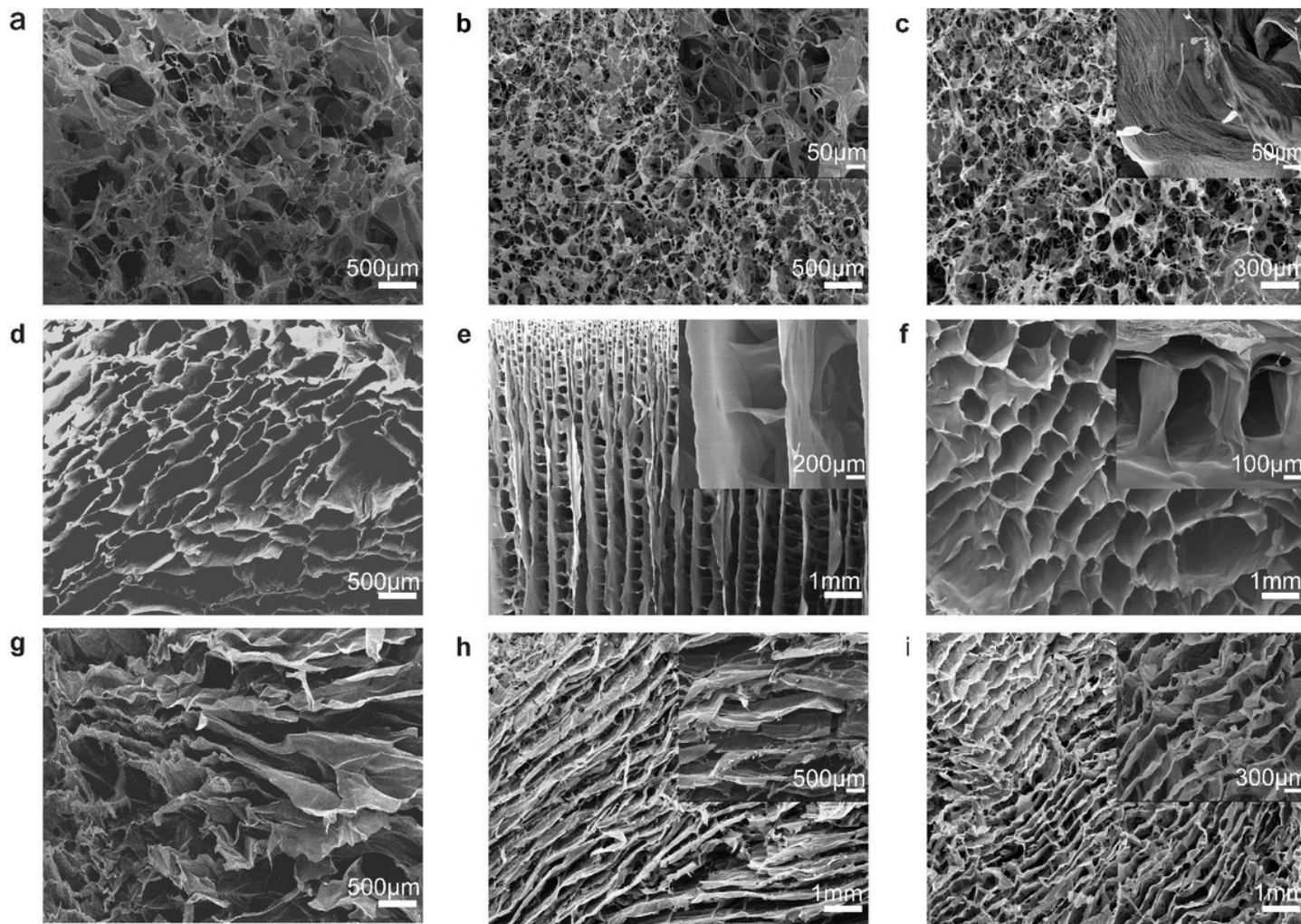


Figure 2

Structural observation of CNF/CS aerogels in the axial and radial direction. a Lower CNF/CS concentrated r-CCSA microstructure. b Axial view of r-CCSA with macrostructure representation. Inset is the SEM images under low magnification. c SEM images for the radial direction of r-CCSA. Inset is the magnification of nanofibers presence on the pore walls. d Lower concentrated u-CCSA lamellas structure. e Axial direction micro-structure representation of u-CCSA with inset of microstructured bridges between lamellas. f SEM images for a radial cross-section of u-CCSA and inset of supportive bridges at high magnification. g Layers' structure of b-CCSA at lower CNF, CS concentration. h Axial orientation of layers in b-CCSA with a inset of high magnification setup of sheets. i SEM descriptions for the radial cross-section of b-CCSA aerogels with inset of macro-orientation of layers with-in geometry

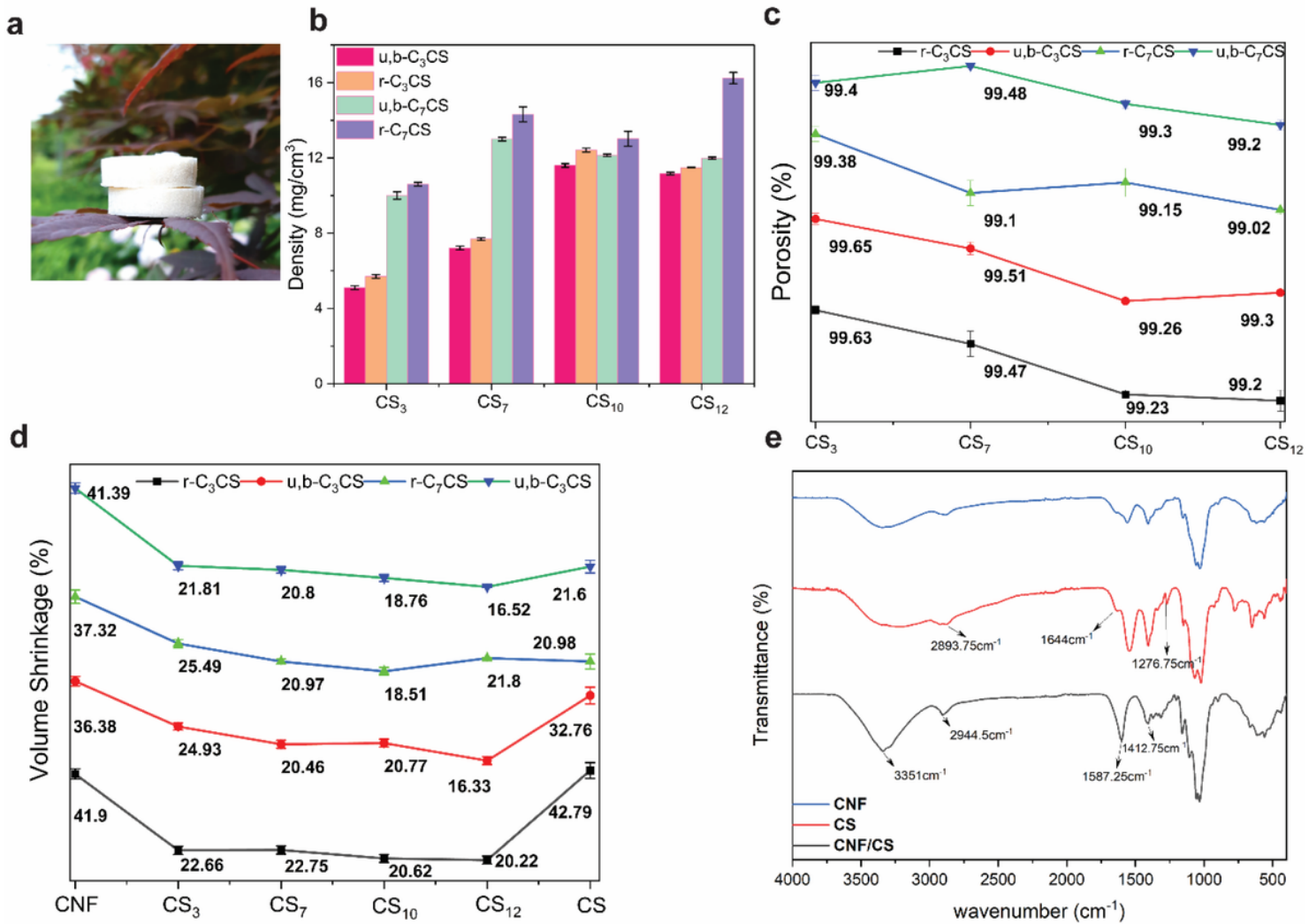


Figure 3

Lightweight CCSAs. a Digital images of lightweight CCSA, captured by keeping them in a stacked form on leaves showing the ultralight formation of aerogels. b The density of compound random (r-CCSA) and anisotropic (u & b-CCSA) aerogels with lower (C3CSA) and higher CNF concentration (C7CSA) combined with CS% of 0.3 (CS3), 0.7 (CS7), 1 (CS10) and 1.2% (CS12) resp. c Porosity percentage of random and anisotropic aerogels with a variation of CNF and CS ratios. d Graphical representation of volume shrinkage rate of pure CNF and CS aerogels, compared with their composites on different ratios. e FTIR spectra of CCSA

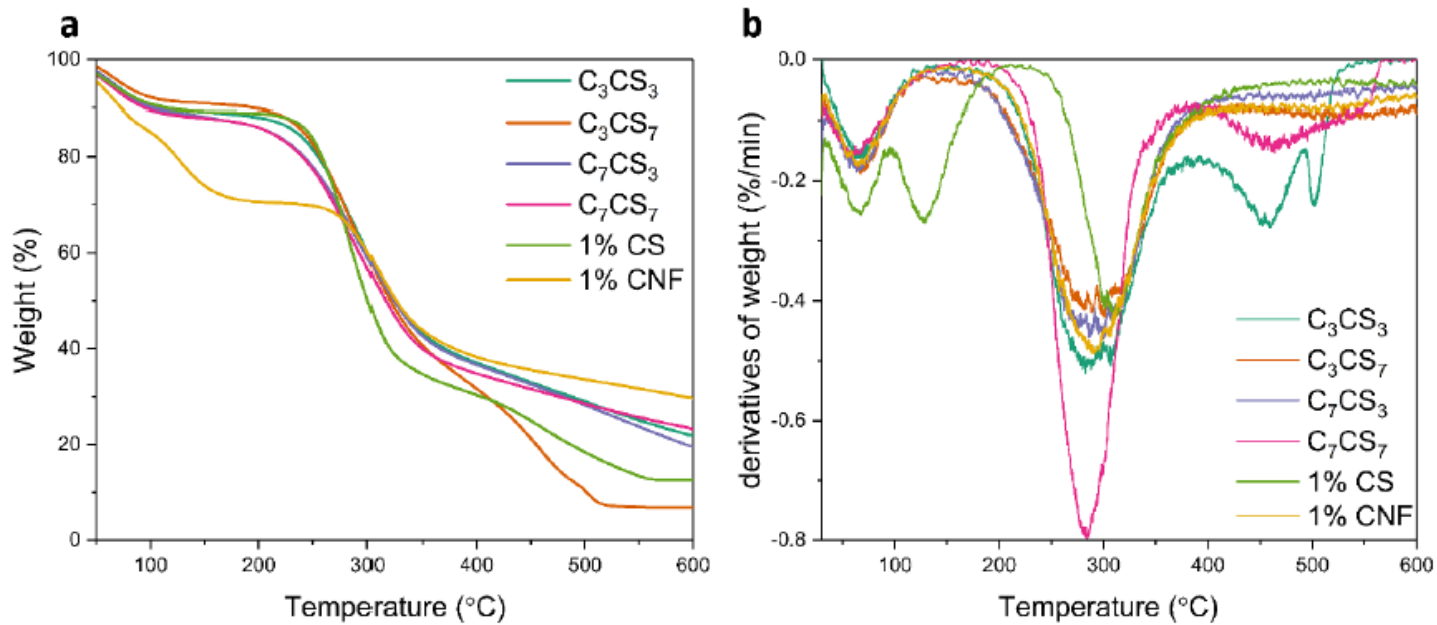


Figure 4

a TGA and b DTG curves of CNF, CS, and their composite aerogels. CS content increased in CCSAs from C7CS3A to C7CS7A exhibit increase in T_g. Less CNF/CS ratio in C3CS3A and shown low T_g

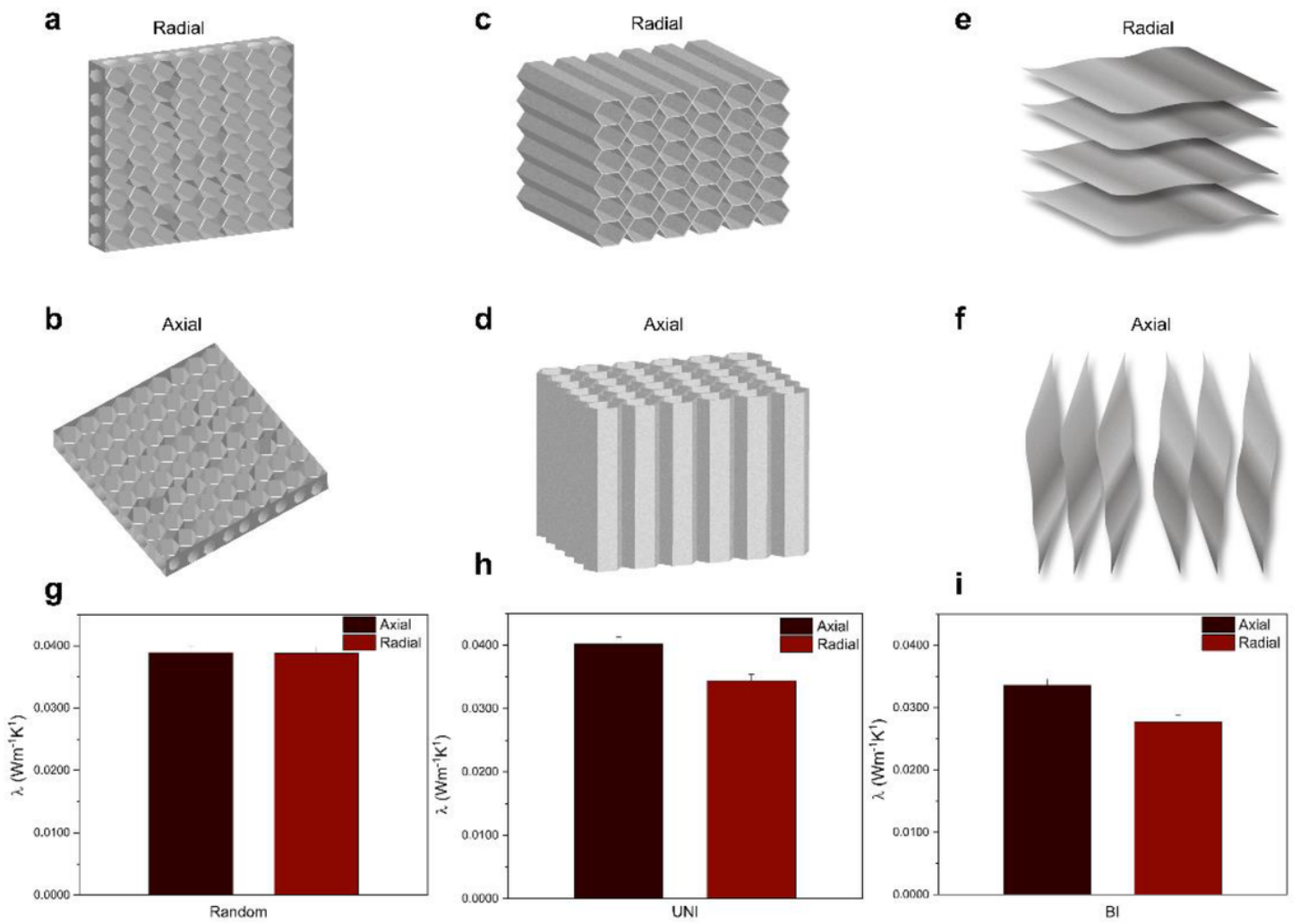


Figure 5

Structural architecture effect on the thermal behavior of isotropic and anisotropic CCSA. Graphic representation for micro-structure of r-CCSA in a radial and b axial direction. schematic illustration for micro-structure of u-CCSA in c radial and d axial direction. Schematic illustrating the microstructure of b-CCSA along e radial and f axial orientation. g Thermal conductivity of r-CCSA. h Thermal conductivity value of u-CCSA. i Thermal conductivity histogram of b-CCSA

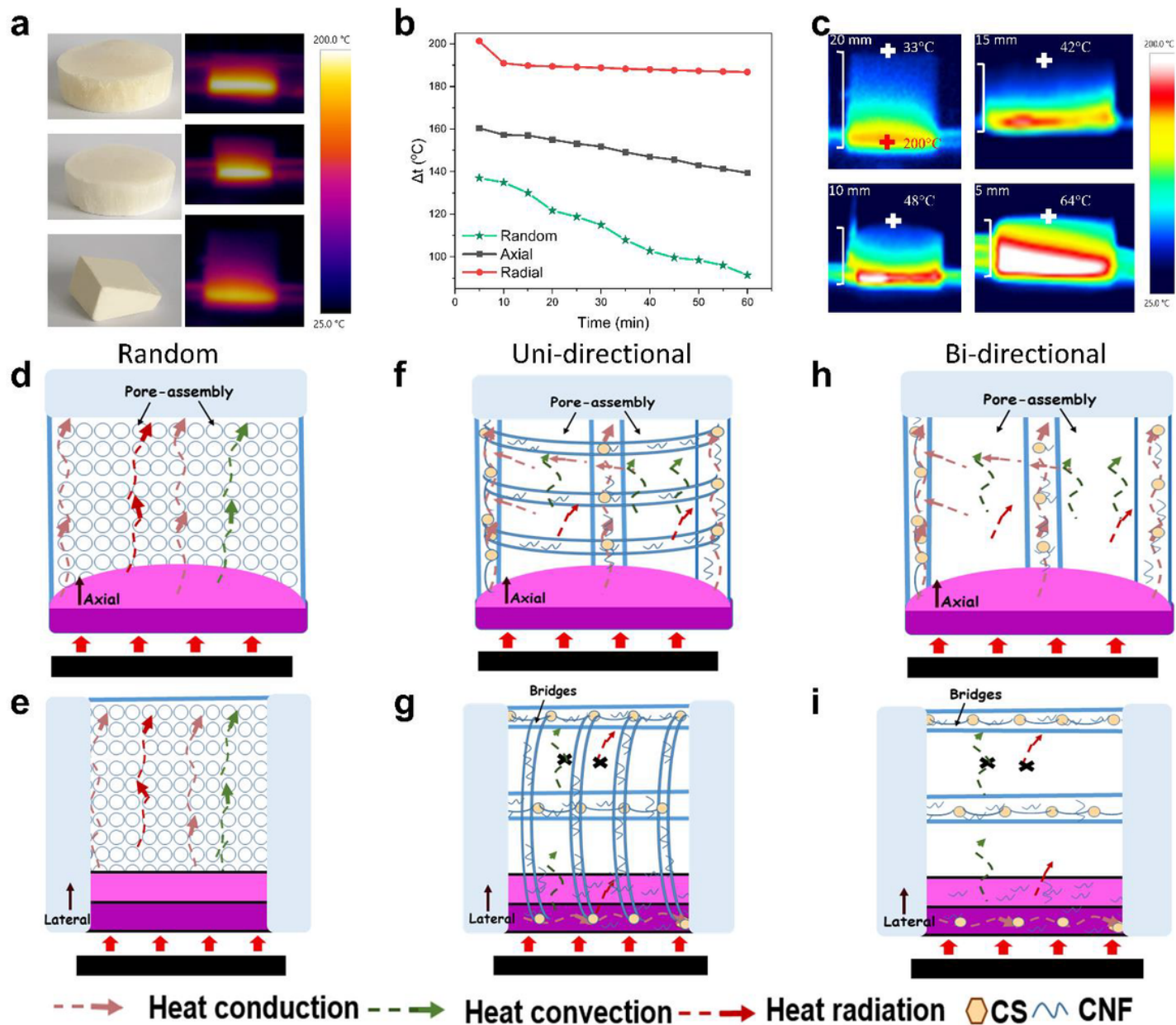


Figure 6

Thermal stability and heat transfer mechanism of CCSA. a Optical and infrared thermal images of r, u, b-CCSA at 200 °C heated plate. b The heat flow pattern of a temperature difference between heated stage and surface of aerogels with different time intervals for 1 hour. c Thermographic images were captured of CCSA with different heights by keeping on a 200 °C hot disk and observation of temperature rise after 10 min. d-i Schematic illustration of thermal insulation mechanism of r,u,b-CCSA in an axial and lateral direction respectively

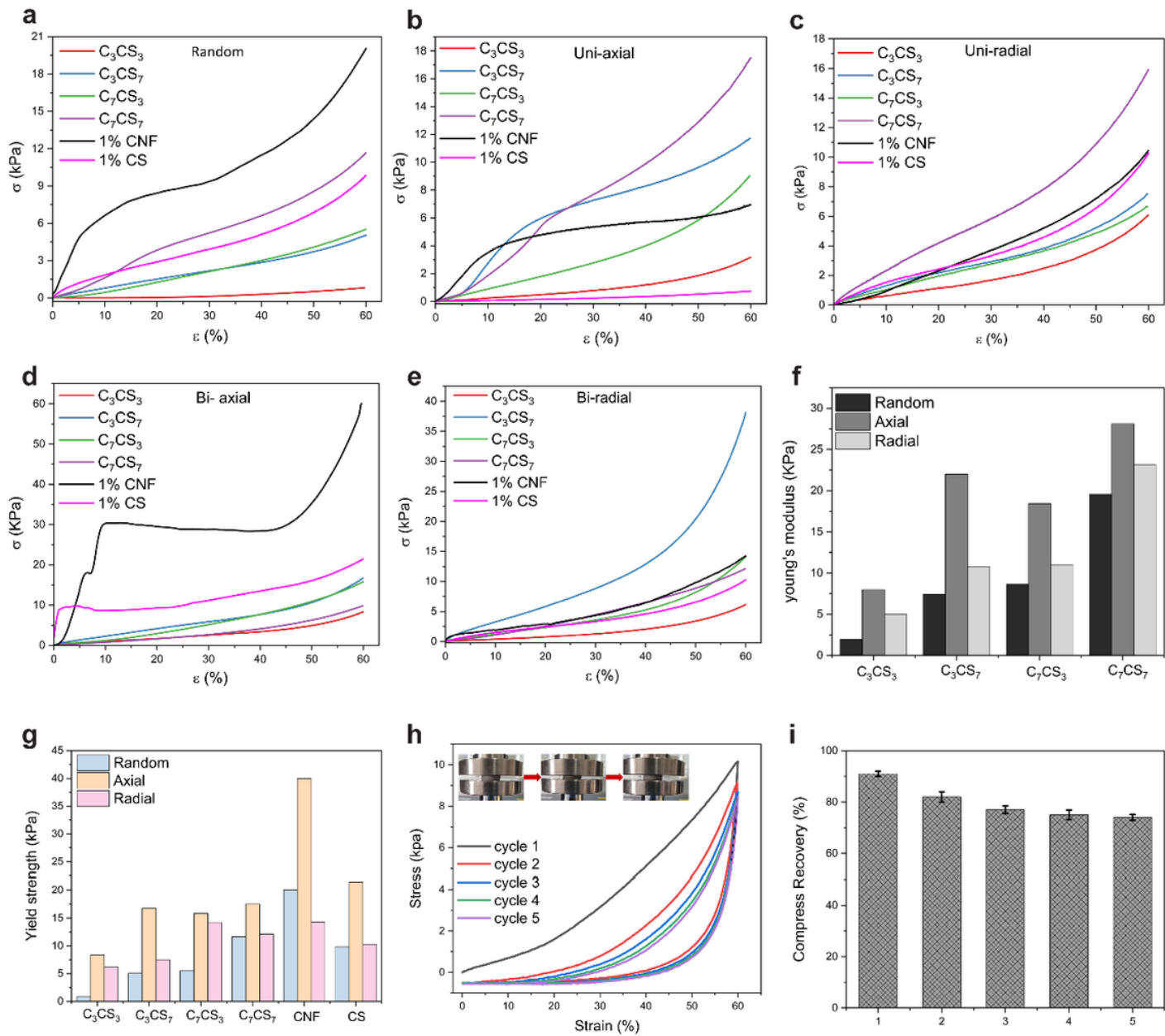


Figure 7

Mechanical behavior of CCSA. a Stress-strain curve of r-CCSA. b Stress-strain curve of u-CCSA along the axial direction. c Stress-strain curve of u-CCSA along the radial direction. d Stress-Strain curve of b-CCSA in an axial direction. e Stress-strain curve of b-CCSA in the radial direction. f Young's modulus histogram of CCSA on various ratios. g Yield strength. h Cyclic loading curve. i Compress recovery at 60% strain

Supplementary Files

This is a list of supplementary files associated with this preprint. Click to download.

- [graphicalabstract.tif](#)
- [ESM1.pdf](#)

- [ESM2.mp4](#)